RESEARCH PAPER

Micromechanical behaviour in shearing of reproduced flat LBS grains with strong and weak artificial bonds

S. S. Kasyap[1] · K. Senetakis[1] · M. R. Coop[2] · J. Zhao[3]

Abstract

The shearing behaviour of reproduced flat LBS grains artificially bonded with ordinary Portland cement (OPC) and plaster of Paris (PP) was examined using micromechanical experiments. Monotonic shearing tests showed a distinct variation in the load–displacement relationship at low, medium and high normal loads, and a nonlinear shear strength envelope was proposed. For OPC-bonded sand grains, a brittle–ductile transition at 20–30 N normal load was observed and three breakage mechanisms in shearing (chipping, shear cracks and crushing) were distinguished in accordance with the changes in the load–displacement curves. OPC-bonded sands showed a predominant dilation at lower normal loads, whereas PP-bonded sands were highly compressive. Based on previously published works using element-scale tests, a new mechanism for dilation under micromechanical testing was proposed in the study. Cyclic shearing tests were conducted on OPC-bonded sands, and the effects of increased displacement amplitude and normal load were highlighted.

Keywords Artificial bonding · Cemented sands · Dilation · Micromechanics · Nonlinear strength

Abbreviations

LBS	Leighton Buzzard sand
PP	Plaster of Paris
LBPP	LBS bonded with PP
NCDT	Non-contact displacement transducer
OPC	Ordinary Portland cement
LBOC	LBS bonded with OPC

List of symbols

F_N	Normal load
$F_{T,PK}$	Peak tangential load
D_T	Tangential displacement
$K_{T,0}$	Tangnetial stiffness at small displacements
D_{cyc}	Displacement amplitude for cyclic shearing
S_q	Surface roughness
F_T	Tangential load
$F_{T,SS}$	Steady-state tangential load
K_T	Tangential stiffness
φ	Friction angle
c	Cohesion
D_N	Normal displacement

✉ K. Senetakis
ksenetak@cityu.edu.hk

S. S. Kasyap
ssarvadev2-c@my.cityu.edu.hk

M. R. Coop
m.coop@ucl.ac.uk

J. Zhao
jzhao@ust.hk

[1] Department of Architecture and Civil Engineering, City University of Hong Kong, Hong Kong, Hong Kong SAR, China

[2] Department of Civil, Environmental and Geomatic Engineering, University College of London, London, UK

[3] Department of Civil and Environmental Engineering, Hong Kong University of Science and Technology, Hong Kong, Hong Kong SAR, China

1 Introduction

Bonding of granular materials either natural, due to precipitation of iron oxide, calcite or silica [37, 45], or artificial, for example for soil improvement purposes [1, 13, 46], alters significantly the mechanical behaviour of the soil matrix. The mechanical behaviour of these bonded grains is influenced by their physical properties,

irrespective of being bonded naturally or artificially [33]. Leroueil and Vaughan [33] also classified cemented sands and weak rocks under the same group of "structured soils". In cemented granular materials, various micro-mechanisms such as cement disaggregation and fragment rearrangement are triggered by relatively small, in magnitude, volume changes of the grain–bond system which lead to significant changes in the response of cemented granular materials and their behaviour is set between classical soil mechanics and rock mechanics [20]. Many researchers have conducted laboratory experiments by means of element-scale tests on artificially cemented soils as for example in the studies by Clough et al. [14], Lade and Overton [30], Coop and Atkinson [16], Haeri et al. [23, 24], Consoli et al. [15], Alvarado et al. [2], Rios et al. [41] and Cui et al. [19]. The key parameters commonly taken into consideration in element-scale tests are the cement type and content, the confining pressure, the porosity of the sample, the stress–strain history and strain level, which collectively determine the strength, breakage mode and yielding of cemented sands.

The variation of peak stress ratio with confining stress for cemented sands is nonlinear, i.e. peak stress ratio increases with decreasing rate [10, 30], and many researchers proposed nonlinear strength envelope models for both cemented and uncemented soils and also jointed and intact rocks [5, 6, 26, 27, 38, 49, 53, 61]. It has been shown in the literature that the classical Mohr–Coulomb failure criterion does not fit well with the failure envelopes of cemented sands which are in general nonlinear in shape. Shen et al. [49] proposed a new approximate nonlinear Mohr–Coulomb shear strength criterion for intact rocks. This approximation provides a piecewise nonlinear envelope considering internal friction angle and cohesion parameters which are dependent on factors such as the level of confinement imposed and the unconfined compressive strength (UCS) of the material. Also, Shen et al. [49] compared their new model with the classical Hoek–Brown (H–B) criterion and stated that the H–B criterion overestimates the stresses at higher confinements, particularly for intact rocks.

The failure mode changes from brittle to ductile as the confining stresses increase [10, 47, 60], and a transition from brittle to ductile nature can be distinctly defined. Also, the dilation tendency, i.e. the stimulus of the cemented materials under low confining pressures to increase in volume, makes their mechanical behaviour rather complex. Laboratory experiments have demonstrated that the presence of cementation or bonding decreases the dilation tendency of cemented materials [3, 35, 47] and that the volumetric behaviour of uncemented and cemented granular materials is different based on the shearing stage. The volumetric behaviour of uncemented sands, i.e. their tendency in dilation or compression, is dependent on the initial state of the soil which is expressed by the combination of the current void ratio and magnitude of confining effective stress [8, 51]. With low effective confining pressures, the post-peak softening of uncemented dense sands is associated with dilation (i.e. increase in volume) [31], while, in cemented sands, the dilative behaviour is initially suppressed by the bonding [35] and when the shearing reaches failure (i.e. breakage of bond), the dilation is higher and mobilizes additional shear strength [30].

There have been extensive numerical studies using the discrete element method (DEM) to investigate various aspects of bonded materials, including strength, bond breakage, brittle–ductile transitions and the influences of bond thickness and confining pressure. These works have revealed the evidenced influence of the particle-scale mechanisms occurring at the contacts of the bonded grains on the bulk behaviour of the material (e.g. [11, 12, 22, 50, 58, 59]). Li et al. [34] compared both experimental and three-dimensional DEM simulation results under triaxial shearing aiming to investigate the effects of different bond strengths on the breakage mechanism of artificially cemented sands. Their study highlighted the formation of shear bands due to local weakness in the sample and the consequent volumetric changes. de Bono et al. [21] conducted DEM simulations on both cemented and uncemented materials using parallel bonds and stated that the cementation increased the brittleness of the numerical samples, while the increase in the confining pressure decreased the influence of the cementation. Wang and Leung [58, 59] highlighted the importance of bond breakage and the dilatancy of cemented materials in their mechanical response by comparing the behaviour between ordinary Portland cement- and gypsum-bonded sand (strong and weak bond, respectively) using parallel and series bonds. Using a biconcave bond model, Chiu et al. [12] provided new insights in linking micro-scale and macro-scale properties of cemented soils. They found that the shape of the bond layer and its thickness are very critical in the stiffness of the bond.

There are, however, rather limited published works performing micromechanical-based experiments on bonded/cemented soils in the literature. An early study by Jiang et al. [29] reported on the response of aluminium alloy rods bonded with epoxy adhesive under combined normal force, shear force and moment, with a primary focus on examining the differences in the mechanical behaviour between thick and thin bonds. Jiang et al. [28] further extended the work to three-dimensional contacts using aluminium hemispheres with elastic properties matching that of quartz sand. These hemispheres were bonded with epoxy adhesive. The effect of normal force on

the peak strengths in shearing, bending and torsional modes was highlighted. Using sand grains bonded with gypsum plaster, Wang et al. [57] examined the cemented particle crushing behaviour by defining different modes of failure. Wang et al. [56] conducted complex loading tests by imposing shearing and combined shearing-bending loads on bonded grains at 50 N normal load. These studies indicated that bond thickness and the morphology of the grains at the boundary with the bonding material are key factors which influence the strength parameters and mechanical behaviour of the specimens.

In the present study, sand grains of very low curvature (or nominally flat grains) were artificially bonded using ordinary Portland cement (OPC) and plaster of Paris (PP) representing strong and weak bonds, respectively, and were further tested under monotonic shearing for a wide range of normal loads. Cyclic shearing tests were also conducted on these specimens at representative normal loads. The experiments were performed using a newly developed micromechanical loading apparatus for cemented grains, which provides high precision of force and displacement increment, and so the quantification of contact stiffness of cemented grains is feasible, overcoming a limitation of the apparatus previously developed by Wang et al. [56].

2 Description of materials and sample preparation

Leighton Buzzard sand (LBS) grains used in the study have sub-rounded to rounded shape and yellow to brown colour. These are typical quartz type grains and were extensively tested in micromechanical experiments published in the literature [40, 44, 48, 55]. The surfaces of these LBS grains were manually flattened using a stainless-steel file which produced very low local curvature and rough profiles, and the grains were bonded in pairs using different cementing agents. The average surface roughness (S_q) of these flat LBS grains was measured for an area of 20 μm × 20 μm, and it was found to be equal to 1400 μm with a standard deviation of ± 200 μm. A typical microscopic image and a surface profile of the flat surface of LBS grains used in the study are shown in Fig. 1a, b. The S_q values are calculated as the root-mean-square deviations of the asperities height with respect to the average (reference) height in the considered area. Such measurements are conducted at 10 different locations for a given specimen, from a set of 10 different specimens making a data set of around 100 different measurements. Two types of cementing agents, which were commercially supplied, were used for bonding the LBS surfaces including ordinary Portland cement (OPC) and plaster of Paris (PP), which would simulate strong and weak bonds, respectively. A cement-to-water

ratio of 0.4 was used for OPC and 0.5 for PP to obtain optimum strength, and these pastes were placed on the bottom flat LBS. Thereafter, the top LBS surface was placed on the cementing agent, and subsequently the grain–cement system (specimen) was allowed to bond naturally. The process was carefully monitored with a digital micro-camera to maintain a thickness of the bond in the range of 0.6–0.8 mm, and the top grain was adjusted for axial alignment within the initial setting time of the cement mortar (less than 30 min). The area of contact was maintained around 6–7.5 mm^2 with a rectangular cross section, measured using image analysis, and any specimens beyond that range were discarded. Once the grains and bonding material were set (initial setting time of 30 min for OPC and 10 min for PP), the OPC-bonded specimens were cured by immersion in water for 24 ± 2 h to attain full 1-day strength of cement mortar, while the PP-bonded specimens were only air-dried at a temperature of 25 °C for 48 ± 2 h. Thus, the system of LBS–Portland cement (denoted as LBOC) represented strong and hard bonded specimens and the system LBS–plaster of Paris (denoted as LBPP) represented weak and soft bonded specimens.

Figure 1c, d shows the spectrum of elements from energy-dispersive X-ray spectroscopy (EDS) analysis of representative samples from the OPC and PP bonds indicating the elements present in both the materials along with scanning electron microscope (SEM) images. These analyses were conducted after the curing/drying period of OPC and PP. PP bonding agent had calcium (Ca) and oxygen (O) as the primary elements with traces of sulphur (S), magnesium (Mg) and various other compounds. OPC bonding agent had a similar composition as the PP bonding agent, with calcium and oxygen dominance with additional small amount of silicon (Si). Unlike the EDS test results, the SEM images (inset of Fig. 1c, d) showed different particle shape and size for OPC and PP materials. PP particles were flaky and had clay-like structures with varied sizes, whereas OPC had angular particles and silt-like structures, and their particle size was larger than PP. OPC showed clusters of particles bonded with matrix, whereas PP had a uniformly distributed matrix of particles.

3 Apparatus and testing program

A new micromechanical apparatus for investigating the behaviour of artificially bonded sand-sized grains under normal, shear and bending loads was developed by Wang et al. [56] at City University of Hong Kong. The apparatus has two loading systems in the vertical and horizontal directions with a linear actuator and a load cell in each direction. Based on these preliminary results and the built of the apparatus by Wang et al. [56], significant
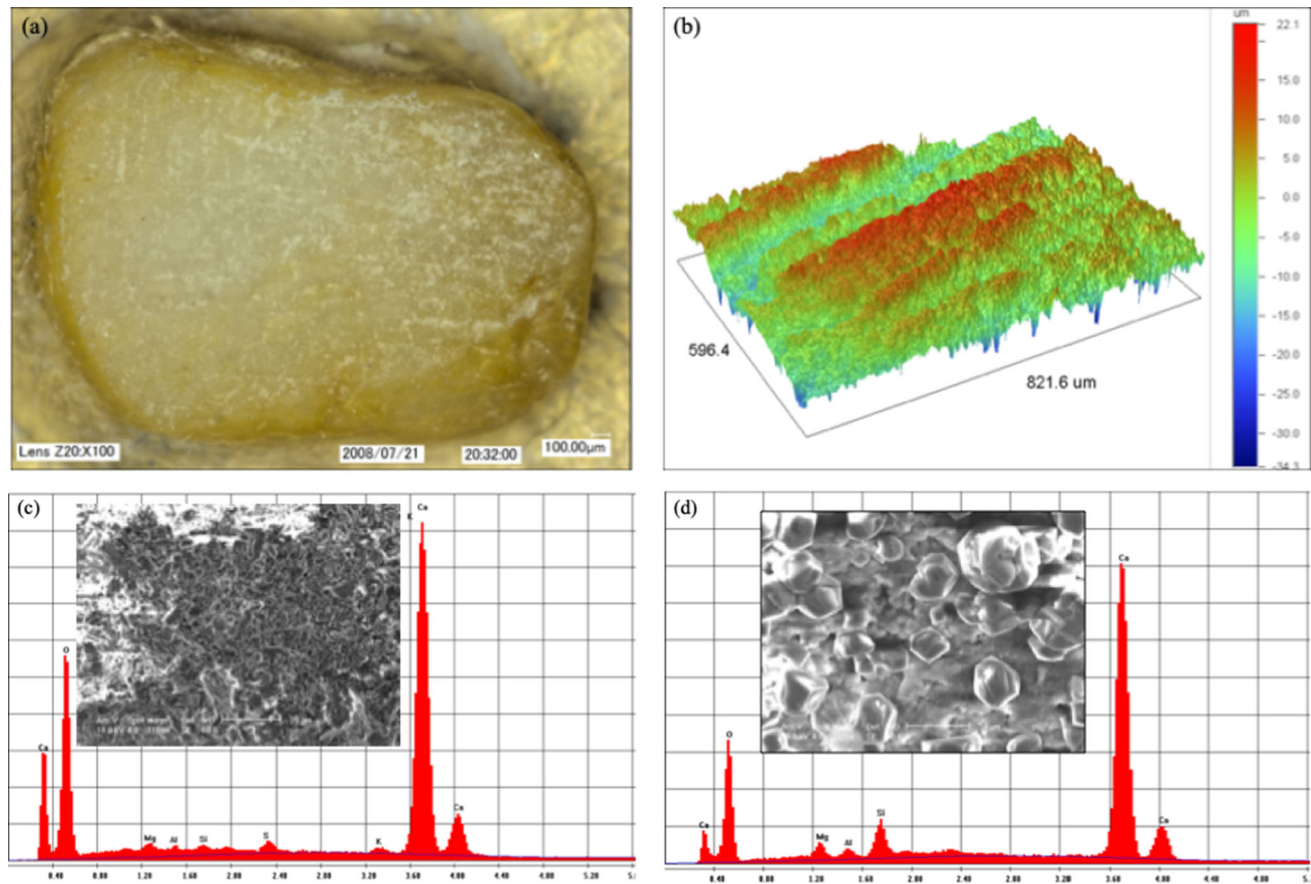
Fig. 1 **a** Microscopic image of top surface of flattened LBS grain; **b** surface profile from interferometry analysis. Representative EDS spectrum of **c** plaster of Paris and **d** ordinary Portland cement with inset of the figures showing SEM images of the corresponding materials

modifications were required, in terms of mechanical arrangement of the apparatus and the testing methodology so that the upgraded apparatus can provide adequate precision of forces and displacements in order to obtain high-quality data in terms of force–displacement relationship and subsequently contact stiffness of the bonded specimens.

The frame of the apparatus was stiffened with four columns with additional brace reinforcement. The effective height of the apparatus was decreased considerably by shortening the connectors at various stages of the loading systems in the horizontal and vertical directions. Linear bearings were used with stiffener plates to guide both the horizontal and vertical motion of the system without any sway, and the restraint of the loading system was improved in each direction. Linear variable differential transformers (LVDTs) were replaced by non-contact displacement transducers (NCDTs), and this further supported measurements of high-precision displacements which are required for calculating contact stiffness. In the upgraded apparatus, a stainless-steel screw shank with lower slenderness ratio was used as the loading arm, with one end being fixed to the load cell through a linear bearing and the other end

being connected to the L-mould using a screw, making it a monolithic structure between the linear actuator and the L-mould. Such an upgrade to the loading arm was needed to increase the stiffness of the apparatus and also to enable the apparatus to carry out cyclic shearing tests. In the previous version of the apparatus by Wang et al. [56], the loading arm was very long ($\sim$ 10 cm) which might induce additional flexibility during shearing. Shortening the loading arm and fixing it at both ends increased the tangential stiffness of the apparatus. Also, the loading arm was not connected to the L-moulds in the previous version. A special frame fixed to the base of the apparatus was used to hold the sensors stationery, and the target for the sensors was fixed to the moving loading arm. The bottom L-shaped mount was fixed to a stainless-steel platform which helped to avoid unwanted movements of the moulds that could disturb the testing process. The upgraded apparatus developed in the present study is schematically illustrated in Fig. 2. The current upgraded version of the apparatus allows the study of combined normal load–shearing, without bending forces, so that at a fundamental level, the interaction of these two forces can be examined. Slight modifications of the apparatus can accommodate further
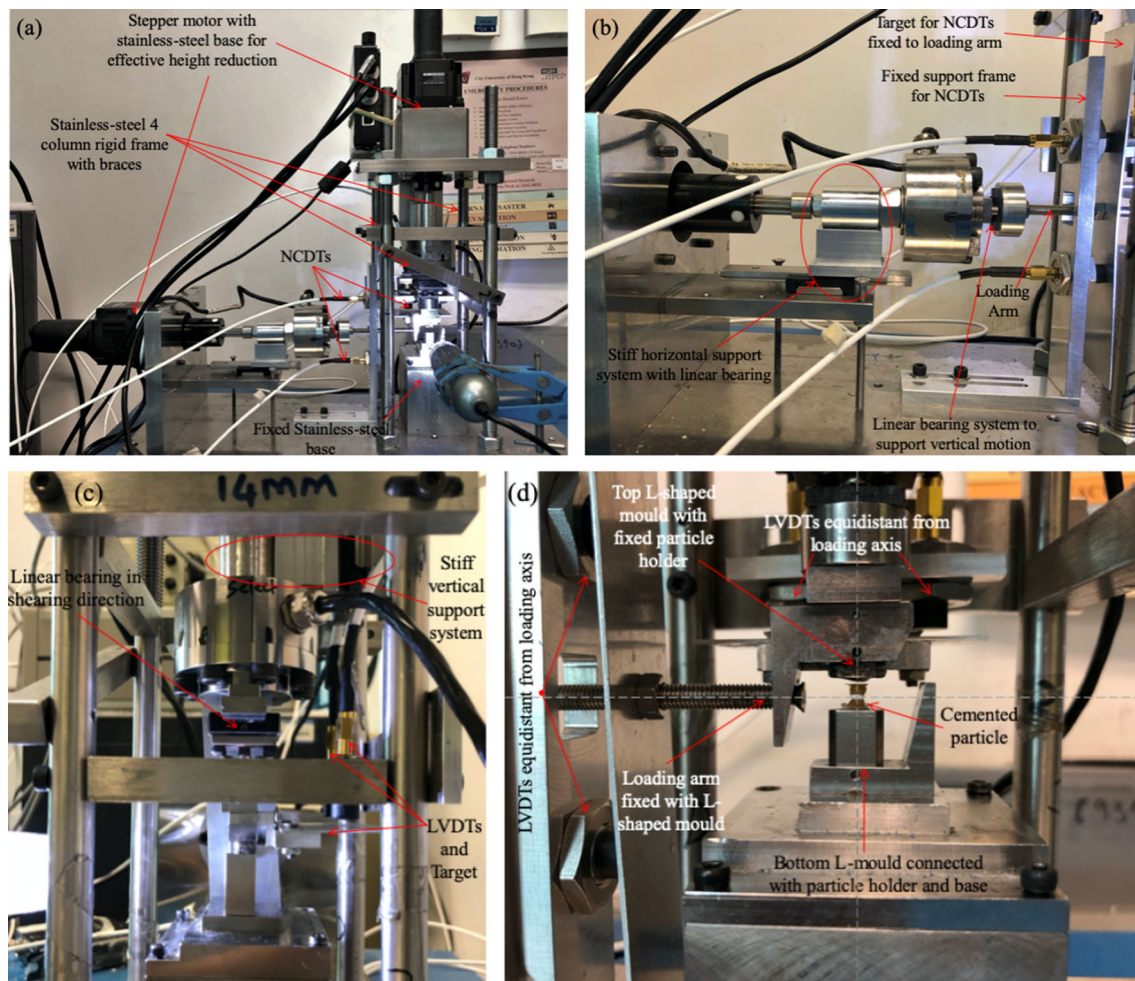
Fig. 2 **a** Upgraded micromechanical testing apparatus for cemented grains; **b** horizontal loading system; **c** vertical loading system; **d** close-up view of arrangement of specimen for testing

application of combined normal–shear–bending forces on the bonded specimens.

The load cells used in the apparatus have a capacity of 1000 N with a factory repeatability of 0.05% FSO (full-scale output) which was further improved after using high-quality signal amplifiers, analogue filters and data logger. The environmental and electrical noise recorded by the load cells is around ± 0.025 N, i.e. ~ 0.003% FSO, which provides results with adequate quality for the range of loads required for tests on bonded grains. Similarly, the environmental and electrical noise of the four NCDTs (non-contact displacement transducers), i.e. two displacement sensors in both the vertical and horizontal directions, was also measured. The average value of NCDT noise varied with a maximum noise of around ± 0.1 μm in both directions.

The test specimens were glued to the top and bottom mounts of the apparatus using a super glue, and they were allowed to dry completely; after the grains were set in position, a nominal normal load was applied to ensure firm contact. Then, the vertical stepper motor was moved downwards to apply the required normal load. Once the normal load was reached, the shearing was applied by horizontally pushing the top L-mould and consequently the top grain moved relative to the fixed bottom grain, applying in this way shearing to the specimen. In monotonic shearing tests, OPC-bonded grains were sheared under constant normal loads ranging from 0 to 100 N for about 300 μm of shearing displacement and PP-bonded grains were sheared for about 200 μm under constant normal loads ranging from 0 to 60 N, so that the effect of confinement on different strength parameters of the bonded grains could be explored. Cyclic shearing tests were also conducted on OPC-bonded grains at 25 N and 50 N constant normal load at different displacement amplitudes. Table 1 provides a summary of the tests.

Table 1 Monotonic shearing test details and results

Bonding material (Code)	Normal load (N)	Tangential load (N)		Load ratio (F_T/F_N)		Dilation (or) compression
		Peak	Steady state	Peak	Steady state	
Ordinary Portland cement (LBOC)	0	5.5	1.8	–	–	Dilation
	2.5	7.5	2.1	3.00	0.84	
	8	11.8	6.5	1.48	0.81	
	16	17.4	9.9	1.09	0.62	
	20	18.8	16.1	0.94	0.81	Post-fracture compression
	25	24.5	21.5	0.98	0.86	
	30	22.2		0.74		
	37.5	29.2		0.78		Compression
	40	26.1		0.65		
	45	30.4		0.68		
	50	32.0		0.64		
	60	42.5		0.71		
	70	37.4		0.53		
	80	41.9		0.52		
	90	48.3		0.54		
	100	44.7		0.45		
Plaster of Paris (LBPP)	0	1.4	0.6	–	–	Dilation
	8	4.4	3.1	0.55	0.39	Compression
	15	8.1	7.4	0.54	0.49	
	20	11.5		0.58		
	25	14.0		0.56		
	32.5	14.2		0.44		
	40	17.3		0.43		
	50	21.1		0.42		
	60	28.5		0.48		

4 Results and discussion

4.1 Monotonic shearing

4.1.1 Tangential load–displacement behaviour

Monotonic shearing tests on LBOC samples were conducted in a wide range of normal loads from 0 to 100 N. The shearing tests at zero normal load (without confinement) indicate the cohesion of the specimens. The shear forces developed in zero normal load tests are due to the combined effect of cohesion and roughness between bounding surface and the bonding agent [53]. Figure 3a, b shows the tangential load–displacement behaviour of both LBOC and LBPP specimens at zero normal load. The LBOC specimens showed a peak tangential load ($F_{T,PK}$) of around 5.6 N and a steady-state tangential load ($F_{T,SS}$) of around 1.85 N, while the LBPP specimens showed lower values than LBOC specimens with $F_{T,PK}$ of 1.44 N and $F_{T,SS}$ of 0.62 N. The softening behaviour or the post-peak

force reduction indicated a force drop (F_d) of around 57% and 67% for LBPP and LBOC specimens, respectively.

Based on the variation of the tangential load–displacement curves, the tests on LBOC specimens were divided into two classes as (1) low–medium range (0–30 N) and (2) medium–high range (40–100 N). This distinction of the tests was based on the linear and nonlinear nature of the initial part of the tangential load–displacement curves (or tangential stiffness variation), the formation of post-peak force reduction, the volumetric behaviour and the brittle–ductile transition zone. Few of these parameters are interlinked, and the details are explained in the subsequent discussions. A limited set of monotonic shearing tests on LBPP specimens was carried out at normal loads ranging from 0 to 60 N, and it was not feasible to make a distinction of the tangential load–displacement curves similar to LBOC. However, an apparent classification was made into low–medium and medium–high normal load cases (8 N to 25 N and 25 N to 60 N, respectively) based on the nonlinearity of the tangential load–displacement curves.

Figure 3c, d shows the tangential load–displacement curves for the low–medium normal load range for LBOC and LBPP specimens, respectively. A very stiff and almost linear increase in the tangential load up to the peak and then a post-peak force reduction occurred for LBOC specimens, but a minor post-peak reduction occurred only at 8 N normal load for LBPP. At other normal loads in the low–medium range of LBPP specimens, the tangential load–displacement behaviour was elasto-plastic with a gradual shift into a steady-state regime. Similar to the zero normal load tests in the previous section, a smooth trend was observed before the steady state and then a rough profile occurred. As the normal loads increased to the medium–high range, the tangential load–displacement curves became nonlinear with hardening behaviour for both LBOC and LBPP specimens and the corresponding curves are shown in Fig. 3e, f, respectively. Occasional stick–slip instability was observed for LBOC specimens, while all the curves for both the specimens showed a rough profile indicating a dominance of friction mechanism over cohesion. Also, the tangential loads mobilized in strong LBOC specimens were higher than the soft LBPP specimens.

4.1.2 Tangential load–normal load variation

The governing factors for the post-peak softening behaviour under low confining pressures for element-scale tests have been mentioned to be the breakage of the cement bridges at lower confinement and the grain crushing and pore collapse at higher confinement [20, 36]. This behaviour can also be correlated with the brittle and ductile failures of the specimens and a distinct transition between the two failure modes (brittle–ductile transition); this problem has been well studied using laboratory element-scale experiments, specifically for bonded grains and rocks [9, 10, 16, 17, 60]. The phenomenon of brittle–ductile transition can be understood from the strength envelopes and the associated failure mechanisms observed in the specimens. Figure 4 shows the variation of the peak tangential load ($F_{T,PK}$) with normal load (F_N) for LBOC and LBPP specimens. For LBOC specimens, the $F_{T,PK}$ values increased with normal load, but at a decreasing rate and a polynomial trendline (dashed lines in Fig. 4) could fit the data with a resultant coefficient of correlation of 0.97 for LBOC test results and 0.99 for LBPP test results.

To further understand the physical meaning of the variation of $F_{T,PK}$ with normal load, a bilinear trendline (P–Q–R in Fig. 4a) was fitted to the datapoints which was optimized for the highest R^2 values, for LBOC specimens. The datapoints at low–medium normal loads were fitted with R^2 of 0.95, and the datapoints at medium–high normal loads were fitted with R^2 of 0.87. This bilinear fitting

helped to differentiate the brittle, ductile and the transition zones as indicated in Fig. 4a. The shaded part in this figure, i.e. F_N = 20–30 N, indicates the brittle–ductile transition for the current state of the LBOC specimens, which would change with bond type and bond thickness. For LBPP specimens, the bilinear trend could not be distinguished to define a brittle–ductile transition. The proposed range of normal loads for brittle–ductile transition in LBOC specimens is substantiated also with the load ratio ($\eta = F_{T,PK}/F_N$) variation as shown in Fig. 4a on the secondary vertical axis. The datapoints of η were fitted with a power function, and the trend of this curve started with $\eta = 3$ at 2.5 N normal load and reached a saturation level of around 0.5–0.6 (53% decrease) beyond the proposed brittle–ductile transition. On the other hand, LBPP specimens showed a 33% decrease in η (0.56–0.4) over the considered normal load range and a power function fitting these data indicated a load ratio saturating at around 0.35.

The variation of peak tangential load with normal load data shown in Fig. 4 has a nonlinear trend, and the data within the given normal load range were fitted using an expression as shown in Eq. (1). This equation was developed based on the framework of Hoek–Brown empirical model for rock samples, translated in terms of loads. Equation (1) depends on the cohesion (C_0) and crushing load (F_C) of the specimens, resulting in tangential load (F_T) at a given normal load (F_N). The coefficient α in this expression is obtained from Eq. (2) using the F_C value of the given specimen type (LBPP or LBOC).

$$F_T = C_0 \left\{ \frac{\alpha F_N}{F_C} + 1 \right\}^{0.7} \tag{1}$$

$$\alpha = 107.4 - 0.42 * F_C \tag{2}$$

"Appendix" explains the details of the crushing test results. Figure 4c shows the fitting of the experimental data with the empirical nonlinear envelope for bonded specimens, and the corresponding R^2 values are also shown in this figure. In Eq. (1), the empirical parameters α and the exponent 0.7 are highly dependent on the crushing loads of the current specimen type, and these both parameters can be understood to be mutually dependent. The trend of strength envelope was with increasing magnitude at decreasing rate, and this suggests that the exponent of the equation must be less than 1. The α value becomes unstable as the crushing strength values increase, and hence extra considerations might be required in both α values and the exponent for different specimens with greater crushing strengths.

4.1.3 Tangential stiffness behaviour

The tangential stiffness (K_T) at a given tangential displacement was obtained by numerical differentiation of the
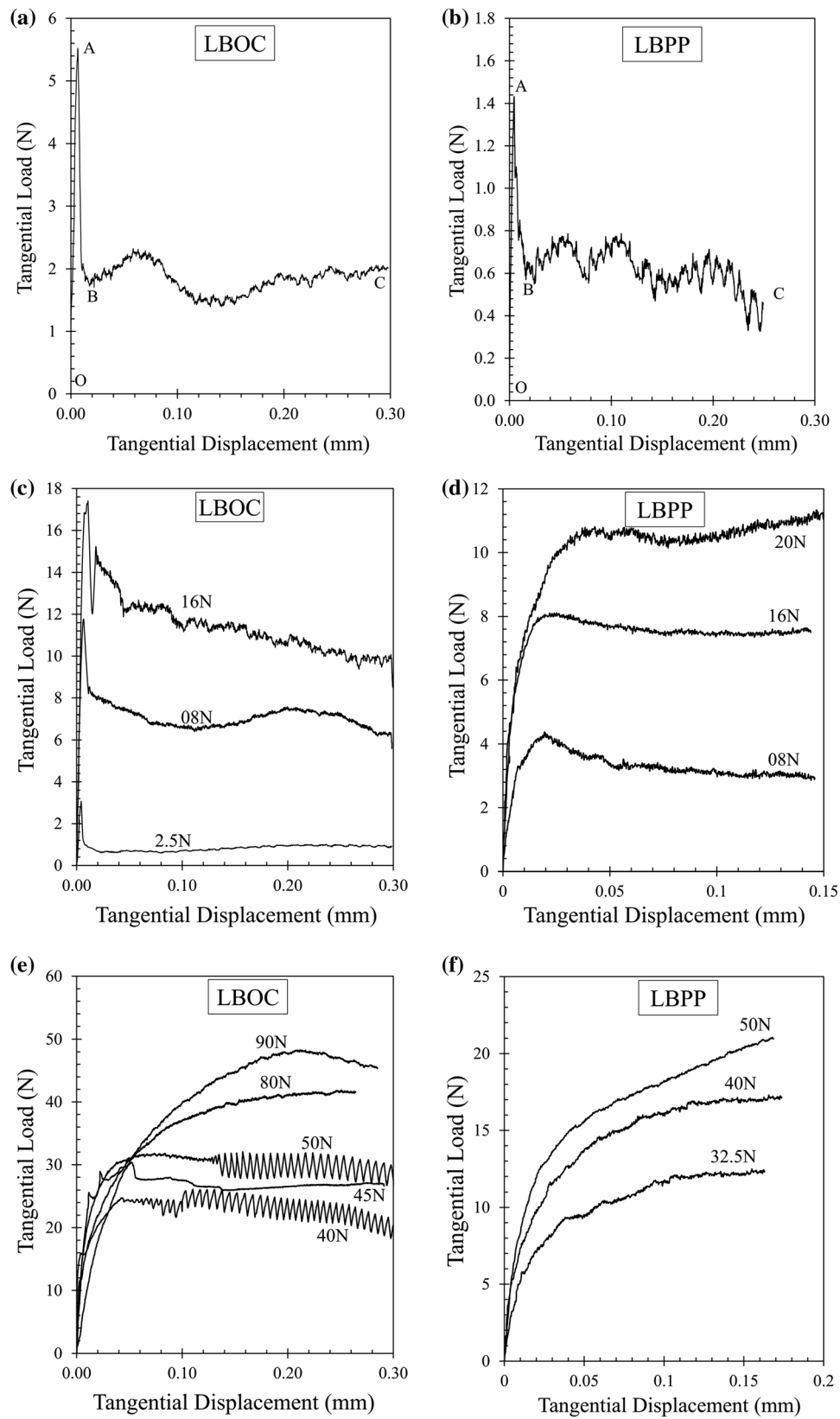
Fig. 3 Tangential load–displacement behaviour of LBOC and LBPP specimens: **a**, **b** zero normal load; **c**, **d** low–medium normal load; **e**, **f** medium to high normal load
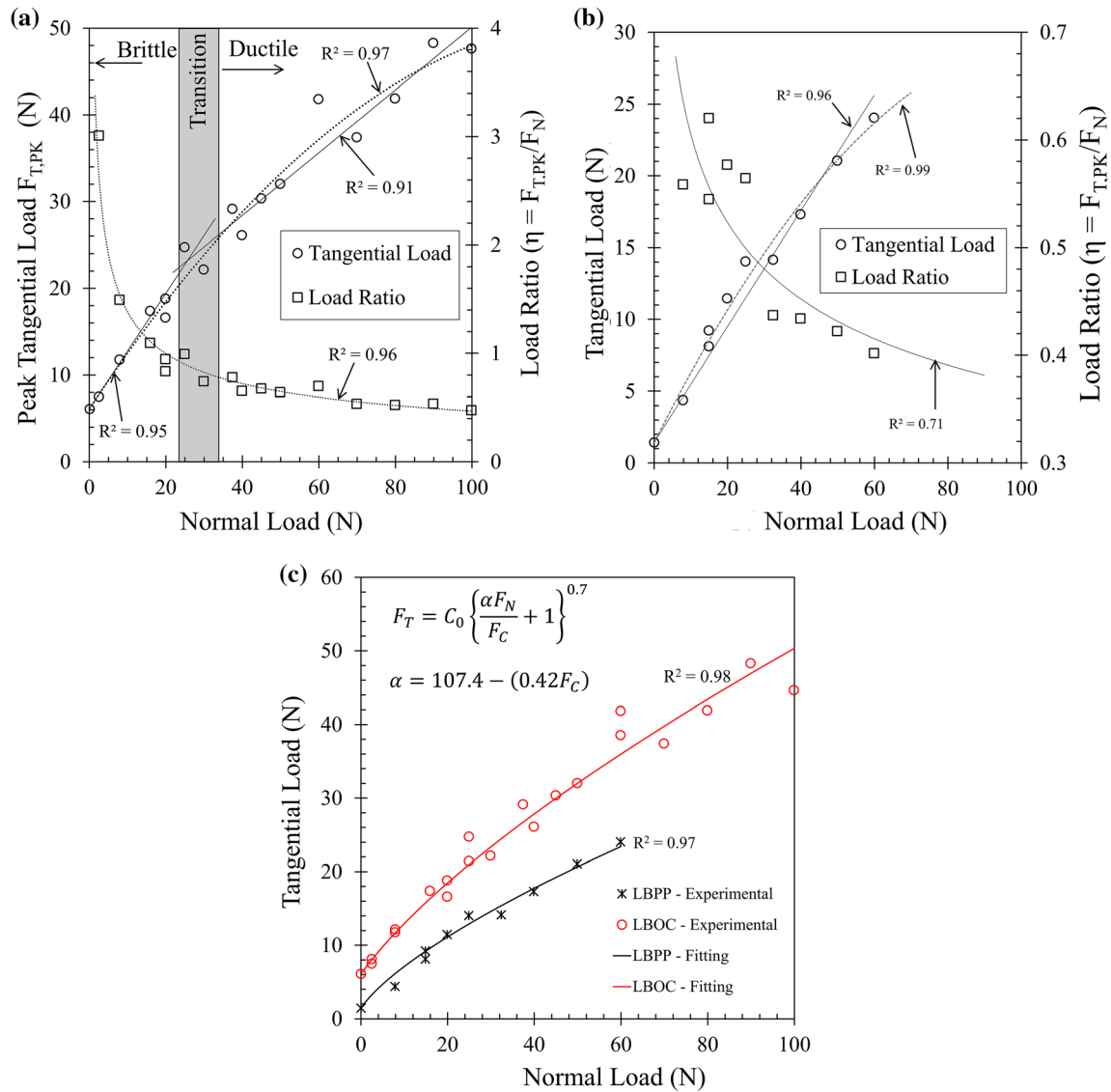
Fig. 4 Variation of peak tangential load (left axis) and load ratio (right axis) with normal load for **a** LBOC and **b** LBPP specimens. **c** Fitting of nonlinear strength envelope for experimental data

tangential load–displacement datapoints. The degradation of tangential stiffness with displacement is highlighted to understand the nonlinearity of the F_T–D_T curves. For LBOC specimens, two classes of stiffness degradation curves were identified based on the applied normal load magnitude, as shown in Fig. 5a, b. In the low–medium normal load range, the stiffness degradation curves were almost horizontal (compared to the extent of degradation in other test cases) for a certain range of tangential displacement and then the curves dropped suddenly to zero stiffness. In the medium–high normal load range, the stiffness degradation curves were highly nonlinear from early stages of the measured displacements. The stiffness degradation curves in both the classes of normal loads showed a few inconsistencies due to the chipping of the

bonding material and early damages occurred in the specimen. However, within the scatter of the data, it was observed that the maximum tangential stiffness values (or initial tangential stiffness, $K_{T,0}$; tangential stiffness value defined at the lowest resolvable tangential displacements) were higher at lower normal loads. Hamidi and Haeri [25] stated that the tangential stiffness of bonded sands becomes close to that of sands without bonds at higher confinements. The $K_{T,0}$ value at $F_N = 8$ N was around 1500 N/mm, and at $F_N = 90$ N, the value was around 2000 N/mm. In the medium range of normal loads, the initial tangential stiffness values increased as high as 10,000 N/mm at around $F_N = 20$–25 N.

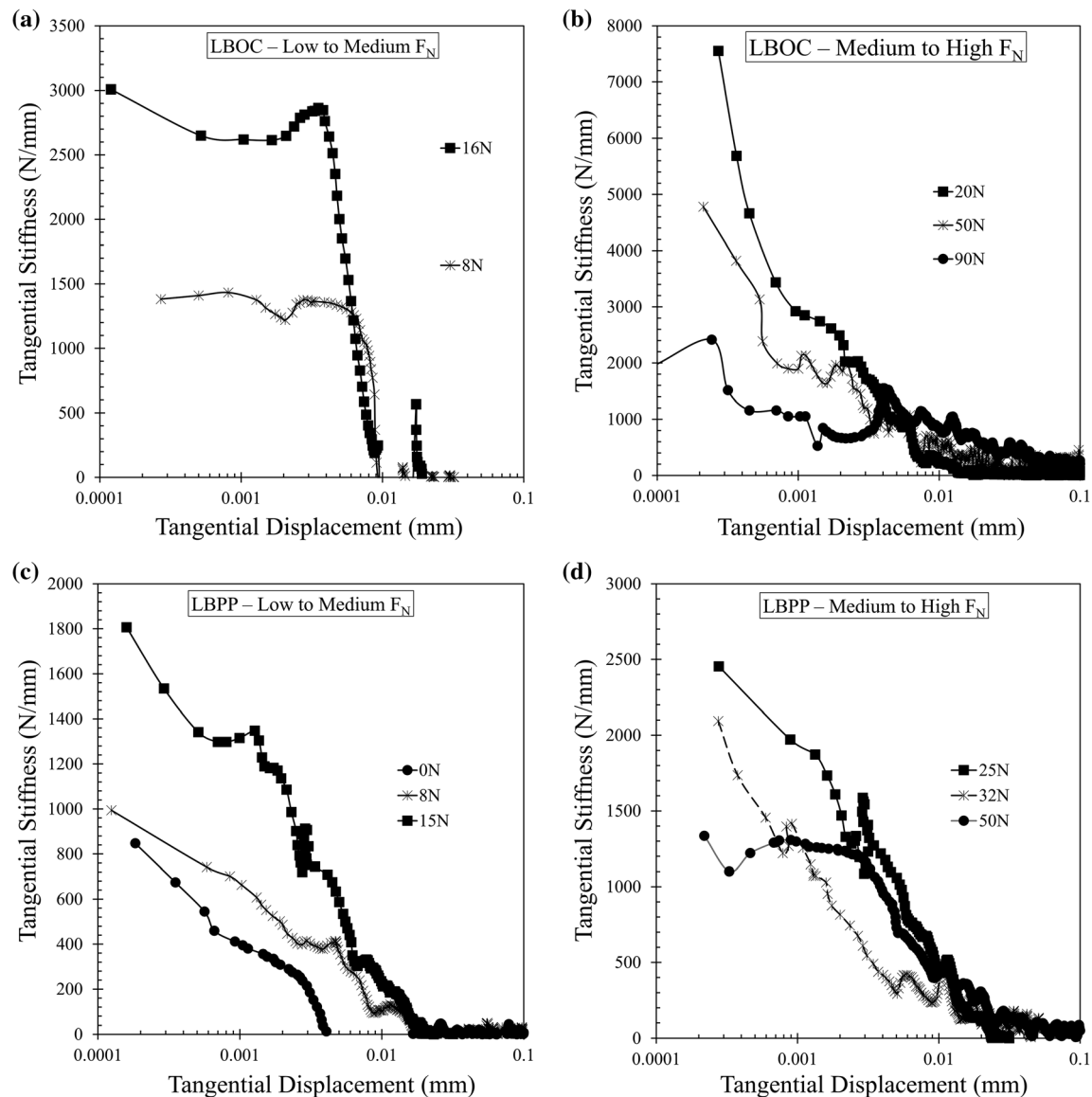The tangential stiffness degradation curves for LBPP specimens did not show such distinction in shape based on

Fig. 5 Tangential stiffness degradation curves for LBOC and LBPP specimens at **a** and **c** low to medium and **b** and **d** medium to high normal loads

the normal load. However, with an increase in normal load the stiffness values decreased and all the curves showed a nonlinear decrease in K_T with tangential displacement. The values of K_T for LBPP specimens were around 2 to 3 times lower than that of LBOC specimens. The stiffness degradation curves for LBPP specimens are shown in Fig. 5c, d.

4.2 Cyclic shearing: LBOC specimens

Cyclic shearing tests of five cycles were conducted on LBOC specimens with displacement amplitude (D_{cyc}) of 10 μm and 25 μm at 25 N normal load and with D_{cyc} of

10 μm at 50 N normal load. These tests give insights into the cyclic shearing behaviour of LBOC specimens at different combinations of normal loads and displacement amplitudes. Figure 6a, b compares the first cycles of tangential load–displacement curves at different F_N–D_{cyc} combinations. Only the 25 N–25 μm test reached steady state and had considerable plastic displacements and energy dissipation in shearing. The 25 N–10 μm test was unloaded at peak load, and hence a smaller amount of plastic displacements was observed, while in the case of 50 N–10 μm test, the maximum tangential load reached was prior to the occurrence of the peak load, resulting in
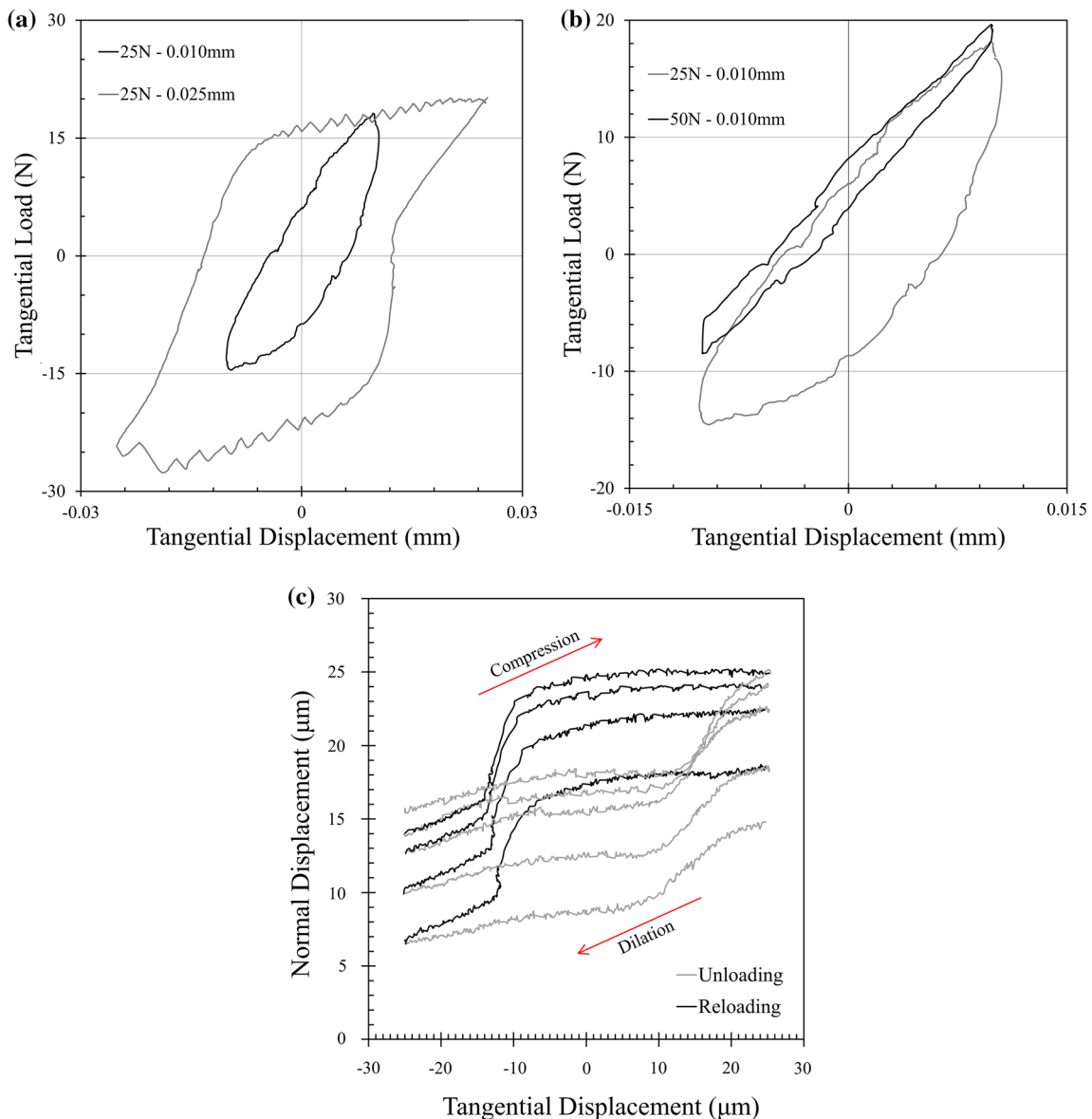
Fig. 6 **a**, **b** Tangential load–displacement curves for first cycle of shearing of LBOC specimens; **c** representative curve of normal displacement versus tangential displacement under cyclic shearing at 25 N normal load

predominantly elastic behaviour with much lesser energy dissipation.

In Fig. 6a, the 25 N–25 μm test showed higher value of maximum tangential load ($F_{T,max}$) in the unloading phase, whereas the $F_{T,max}$ value in the loading phase was the same as in the 25 N–10 μm test. This can be explained from the volumetric behaviour of the specimen in the loading and unloading phases. Figure 6c shows the variation of D_N with D_T, where the curve shows dilation in the unloading phase (backward shear) and compression in the loading/reloading phase (forward shear). The fracture developed in the bonding of the specimen closes while unloading (backward shear), and the blocks of the bonding material on either

sides of fracture tend to slide against each other. The generated dilation and frictional behaviour in the specimen (Video S1) lead to the excess mobilization of tangential loads as shown in Fig. 6a. In the reloading phase, the crack opens and propagates the already existing crack, leading to peak tangential load similar to that of the 25 N–10 μm test. This phenomenon continues through the five cycles of shearing with decreasing amplitudes of dilation and compression as shown in Fig. 6c. Figure 7a–c shows the five cycles of hysteretic loops for the three classes of tests. For 10 μm tests, the hysteretic loops showed no significant plastic deformations and hence the secant stiffness (slope of hysteresis) can be considerable. For the 25 N–25 μm
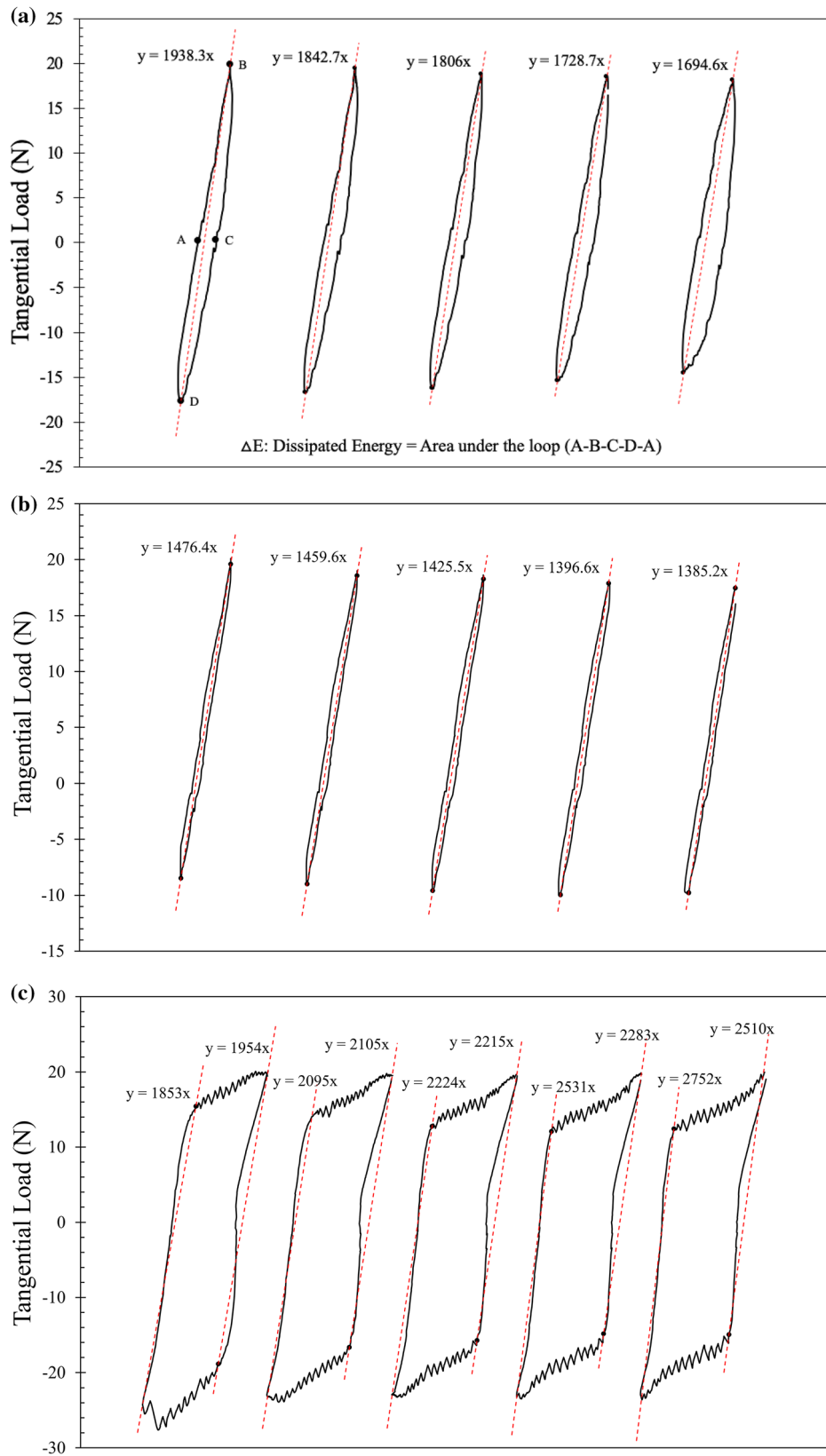
Fig. 7 Tangential load–displacement curves under five cycles of shearing **a** 25 N–0.01 mm; **b** 50 N–0.01 mm; **c** 25 N–0.025 mm

test, the elastic stiffness can be approximated from the slope of loading and unloading parts of the curves as indicated in Fig. 7c.

The dissipated energy is generally an indicator of the frictional losses in the contact of two bodies and is calculated from the area of the closed loop in a cyclic loading process. In the case of bonded grains, the adhesive forces also compensate for the energy losses in cyclic shearing. These losses include the elastic or plastic nature of opening and closure of microcracks in the process of cyclic loading. The difference of dissipated energy (ΔE) values in the three test cases, as shown in Fig. 7, is more than one order of magnitude. The trend of dissipated energy is similar to the trend of slope of hysteresis, with the 25 N–25 μm case dissipating the maximum and the 50 N–10 μm case dissipating the minimum. However, there were observed differences with increasing number of cycles within each test case and this variation is shown in Fig. 8a. Bar graphs in this figure indicate the ratio of the dissipated energy in each cycle to the first cycle of shearing, and their numerical values are shown in Table 2. At a given normal load of 25 N, the two displacement amplitude cases showed significant differences in the dissipated energy values. In cycle 1 of shearing, the dissipated energy for 25 N–10 μm case was around 0.16 N-mm, while the 25 N–25 μm case had a corresponding value of 1.12 N-mm, which is around seven times higher than the former case. With 10 μm of D_{cyc}, the curves are still in the elastic region of behaviour and hence the values of dissipated energy are smaller than the 25 μm case where the curves entered the plastic deformation stage. Also, with the number of shearing cycles the trend was different for lower and higher displacement amplitudes. With 10 μm of D_{cyc}, at both 25 N and 50 N normal load, the ΔE values increased by around 1.3 times (30% increase) from cycle 1 to cycle 5, which can be understood as increased frictional losses incurred by the damage of the bonding agent (discussed later in this section). On the other hand, with 25 μm of D_{cyc}, the ΔE values decreased by around 0.1 times (10% decrease) from cycle 1 to cycle 5, as the specimens are well within the elastic region and so no damage was propagated with the increase in shearing cycles.

The hysteretic damping ratio values are calculated based on the elastic energy stored in each cycle, and the variation for three test cases and five cycles of loading is shown in Fig. 8b. The damping ratio values are also shown in Table 2. The variation of damping ratio was similar to the variation of dissipated energy values as shown in Fig. 8a and Table 2 with 25 N–25 μm case showing the maximum damping due to the induced plastic deformations.

From one cycle to another, the slope of hysteresis showed a decreasing trend, but the variation was smaller in all the test cases. As the loading cycles increased, microcracks in the cemented specimens were generated and this

decreased the load carrying capacity (combined stiffness in loading and unloading) of the specimens. The tangential load amplitude ($F_{T,Amp}$) is the summation of the maximum tangential loads attained in loading and unloading phases of each cycle. The variation of $F_{T,Amp}$ is shown in Fig. 8b with bar graphs. The 25 N–25 μm test showed the maximum value, and the 50 N–10 μm test showed the least. This is expected since the 50 N–10 μm test did not reach its peak load in the loading phase, and thus it remained in a relatively elastic state unlike the 25 N normal load test. Also, the attenuation of $F_{T,Amp}$ with increasing cycles was higher for the cases where ductile behaviour was the dominant, i.e. at 25 N normal load. The 25 N–10 μm and 25 N–25 μm tests showed an attenuation of 10% to 13% of $F_{T,Amp}$. The consequences of this damage were explained in terms of energy dissipation using Fig. 8a. Also, the tangential load values reflect the damage developed in the bonding agent. During the first cycle of shearing under 25 N–25 μm case, the $F_{T,Amp}$ value was the highest at 47.8 N where the major damage (or shear crack) was observed. In the consecutive cycles, lower $F_{T,Amp}$ values (~ 43.5 N) were recorded as either the existing crack/damage was propagating or new cracks (only minor) were developing during shearing.

After the first cycle of tangential loading and unloading, a macroscopic failure was observed in the 25 N–25 μm test (Video S1). Opening and closure of the crack(s) allowed the specimen to dissipate the energy through this process, leading to a maximum energy dissipation and tangential load amplitude and a minimum hysteresis slope. In other tests at lower displacement amplitude (10 μm), no visible cracks/failures were observed. However, decreasing stiffness and tangential load amplitude imply that some microcracks were developed in the cementation of the specimens. With the number of shearing cycles, the damage was induced in the cementation by either propagation of microcracks and/or formation of new microscopic cracks.

4.3 Dilatancy and breakage mechanisms

4.3.1 Influence of normal load on dilatancy

After Rowe [42] and Rowe et al. [43], the relation between stress and dilatancy for cemented sands has been studied extensively in the literature [16, 18, 47, 52, 54, 62]. The breakage mechanism also depends on the magnitude of the normal load. Since the bonding is brittle, cohesion dominates at lower normal loads and the specimen will have brittle breakage. At higher normal loads, the cohesion between the grains becomes a less influential factor and friction carries the tangential loads leading to ductile breakage of the specimen.
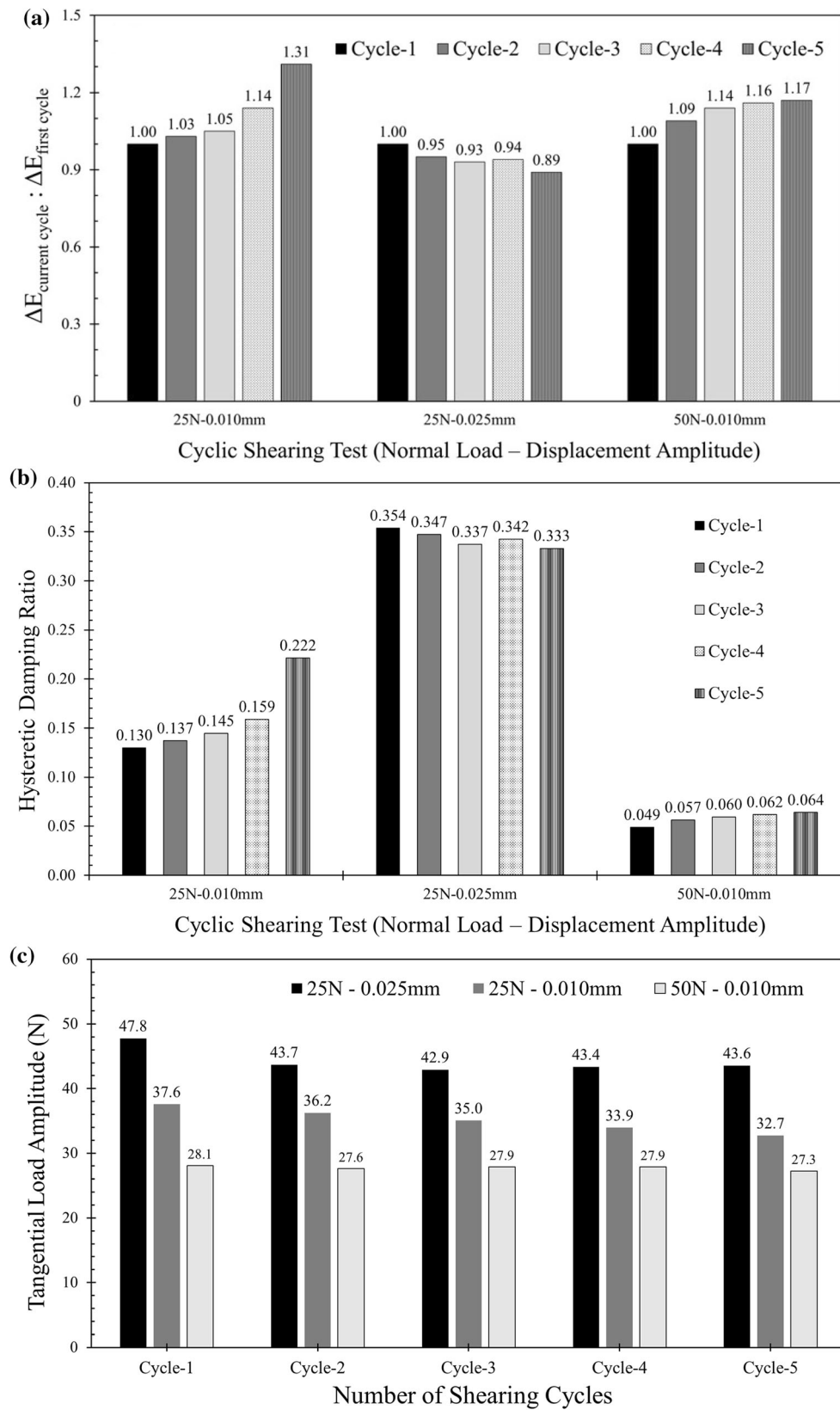
Fig. 8 **a** Variation of ratio of energy dissipated in a cycle to first cycle of shearing; **b** variation of hysteretic damping ratio from cycle to cycle at three test conditions; **c** variation of tangential load amplitude from cycle to cycle

Similar to the expected macroscopic behaviour of granular materials (e.g. [4, 18, 39]), the present micromechanical experiments also showed dilative behaviour at lower normal loads and compressive behaviour at higher normal loads for bonded sand grains. The rigid loading arm for shearing is connected to a linear bearing at the farther end to accommodate the vertical movements (Fig. 2b), and the measurement of vertical displacements during shearing is feasible. The dilative or compressive behaviour of LBOC specimens reciprocated with their breakage mechanism based on the magnitude of the applied confinement.

Figure 9a shows the variation of vertical displacement, i.e. dilation (−ve) or compression (+ve), with shearing displacement for LBOC specimens at different normal loads. It is evident that as the confinement (or normal load) increases, the behaviour is shifting from pure dilation to pure compression. The tests with normal load lower than 20 N showed pure dilative behaviour with maximum dilation of around 72 μm at 0 N normal load. (Note that the terms "dilation" and "compression" are discussed in the study by means of vertical displacement with positive values denoting compression.) The maximum compression was around 140 μm at 100 N normal load test. At the normal load range of the proposed brittle–ductile transition (i.e. 20–25 N), the tests showed minimum change in the vertical displacement. The inset of Fig. 9a shows the vertical displacement variation for 20 N normal load case. The curve showed pure dilative behaviour in the beginning and later started to show compressive behaviour. This is related to the breakage of the bonding between the LBS grains as it will be discussed later in this section.

Figure 9b shows a representative test at F_N = 8 N comparing the variation of tangential load, normal load and normal displacement with shearing displacement. The normal displacement curve showed a dilative behaviour apart from a small initial compressive stage, and the slope of the curve (rate of dilation) changed at the start of the steady state. The rate of volumetric change (i.e. slope of the volume change versus tangential displacement) is also maximum at a tangential displacement where the corresponding tangential loads started to decrease from their peak value. Similar observation was reported by Wang and Leung [59] from triaxial compression tests on Ottawa sand mixed with cement slurry. Figure 9c shows the variation of the rate of dilation with tangential displacement for representative tests at low, medium and high normal loads. At lower normal loads, the rate of dilation was negative and was maximum during the peak load and then it tended to reduce to zero during the later stages of shearing. At medium normal loads, the curves showed almost zero dilation rate until breakage occurred in the cementation and then they showed compressive behaviour (i.e. positive rate of dilation). The higher normal load tests showed purely compressive behaviour with a constant value of positive rate of dilation.

4.3.2 Breakage mechanisms

Three modes of breakage were observed in the specimens (1) chipping and specimen separation (at lower normal loads), (2) shear cracks and splitting (at medium normal loads) and (3) crushing (at higher normal loads). All these

Table 2 Observations from cyclic shearing tests on LBOC specimens

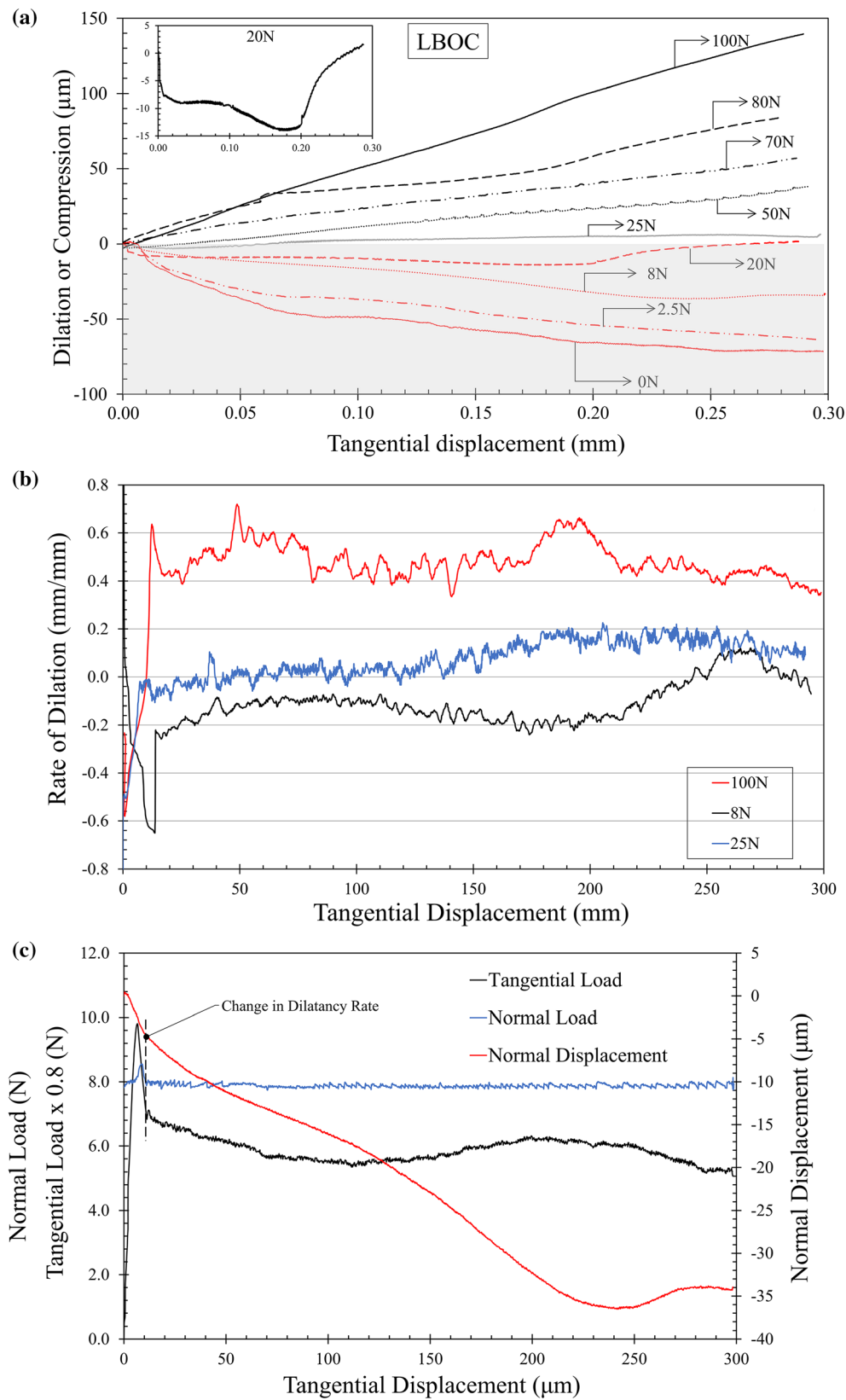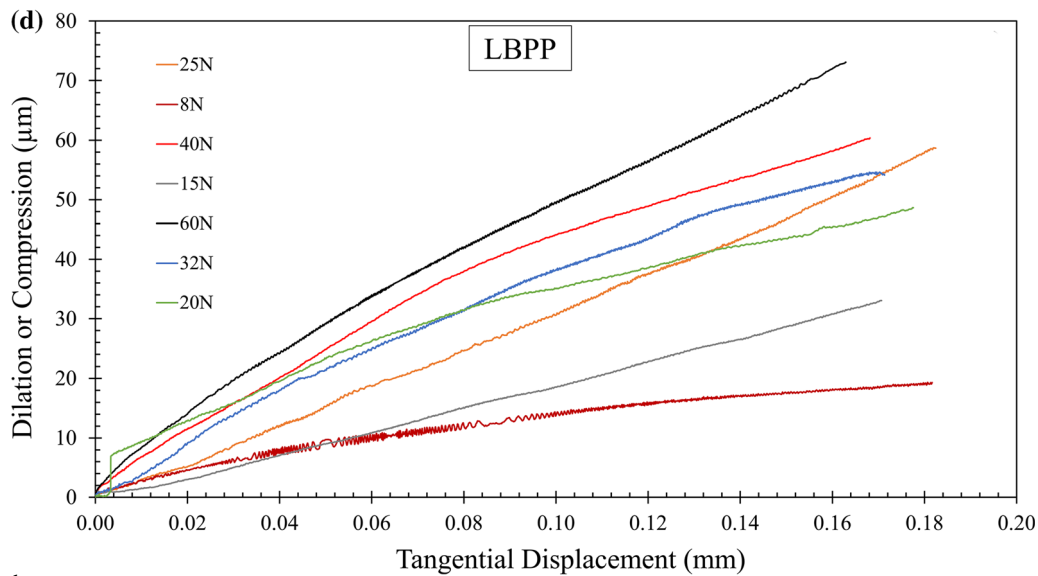| Normal load (N)	Displacement amplitude (mm)	Cycle	Energy dissipated (N-mm)	Damping ratio	Stiffness (N/mm)	Load amplitude (N)
25 N	0.010	1	0.1628	0.130	1938.3	37.56
		2	0.1678	0.137	1842.7	36.24
		3	0.1708	0.145	1806	35.03
		4	0.1851	0.159	1728.7	33.93
		5	0.2526	0.222	1694.6	32.71
25 N	0.025	1	1.1193	0.345	1903.5	47.8
		2	1.0661	0.347	2100	43.7
		3	1.0420	0.337	2219.5	42.9
		4	1.0466	0.362	2407	43.4
		5	0.9962	0.333	2631	43.6
50 N	0.010	1	0.0602	0.049	1476.4	28.08
		2	0.0660	0.057	1459.6	27.6
		3	0.0684	0.060	1425.5	27.88
		4	0.0696	0.062	1396.6	27.87
		5	0.0703	0.064	1385.2	27.25

Fig. 9 **a** Variation of normal displacement (dilation or compression) with shearing displacement at different normal loads for LBOC specimens; **b** comparison of variation of tangential load, normal load and normal displacement with shearing displacement for $F_N = 8$ N test; **c** variation of rate of dilation or compression with shearing displacement; **d** variation of normal displacement (dilation or compression) with shearing displacement at different normal loads for LBPP specimens

◀**Fig. 9** continued

three phenomena were observed only in the bonding material, and the sand grains showed no signs of failure. Wang et al. [56] stated that shearing tests of LBS grains bonded with gypsum plaster at $F_N = 50$ N showed yielding at 21 N and the failure was attributed to the rotation of the whole specimen about the bottom sand particle without any visible cracks.

Mode-1: Chipping and specimen separation type of failure was observed in specimens sheared at lower normal loads ($F_N < 20$ N). Figure 10a shows the three stages of a specimen sheared at $F_N = 8$ N i.e. the initial stage after the application of normal load, chipping during shearing and clean separation of specimen after the removal of the normal load. The high dilatancy at low normal loads in the current set of specimens indicated the mechanism of failure and energy dissipation. During shearing, the specimens with low confinement tended to dissipate energy by bond splitting rather than shearing along the bond (weakest link in the specimens). In the process of bond splitting/specimen separation, the specimens showed significant dilation while shearing due to uplift tendency (i.e. termed as dilation) of the top grain. At the interface of the bonding material and the grain, a slight chipping was observed while shearing and this is shown in Video S2. Once the complete separation occurred, the dilation rate reached zero and the friction became the dominant mechanism of shear strength, overtaking cohesion and dilation counterparts.

Mode-2: Shear cracks and splitting type of failure was observed in specimens sheared at the medium range of normal loads ($F_N = 20$ N–30 N). Video S3 shows the failure of a specimen with shear cracks and splitting occurring in the bonding material. These are only the visible failures observed in the specimens, but many

microscopic cracks are expected in the sample which would lead to the failure of the specimen. This type of failure is a special case since the normal load pertaining to this class was proposed to be brittle–ductile transition in the previous sections. In these specimens, the dilation rate was almost zero and the shear cracks in the specimen showed a distinctive phenomenon in the tangential load–displacement curves. Figure S1 shows the tangential load–displacement curves at 20 N and 25 N normal loads. During the peak tangential load, no cracks were visible in the specimen, but during the steady-state shearing the cracks started to expand and later a sudden drop in tangential load was observed (as indicated in Figure S1). This is the point where the specimen started to show compressive behaviour from zero dilation condition as indicated in the subset of Fig. 9a. These shear cracks were always inclined in the direction of shearing at an angle of 50° to 60° with respect to the horizontal.

Mode-3: Crushing type of failure was observed in the specimens sheared at higher normal loads ($F_N > 50$ N). Crushing was observed only in the bonding material, and the crushing behaviour of the specimens at 90 N is shown in Video S4. At this high normal load, the stresses created in the specimen are almost nearing to one-day crushing strength of cement mortar and due to the imposition of shearing the bonding material loses its strength to resist. In this stage, the specimens showed pure compression in the normal displacement against tangential displacement curves. However, the crushing failure mechanism was not reflected in the tangential load–displacement curves as in the shear cracks mode, except for the delayed stiffness degradation and highly nonlinear curves.

The LBPP specimens showed purely compressive behaviour except for zero normal load shearing. Figure 9d
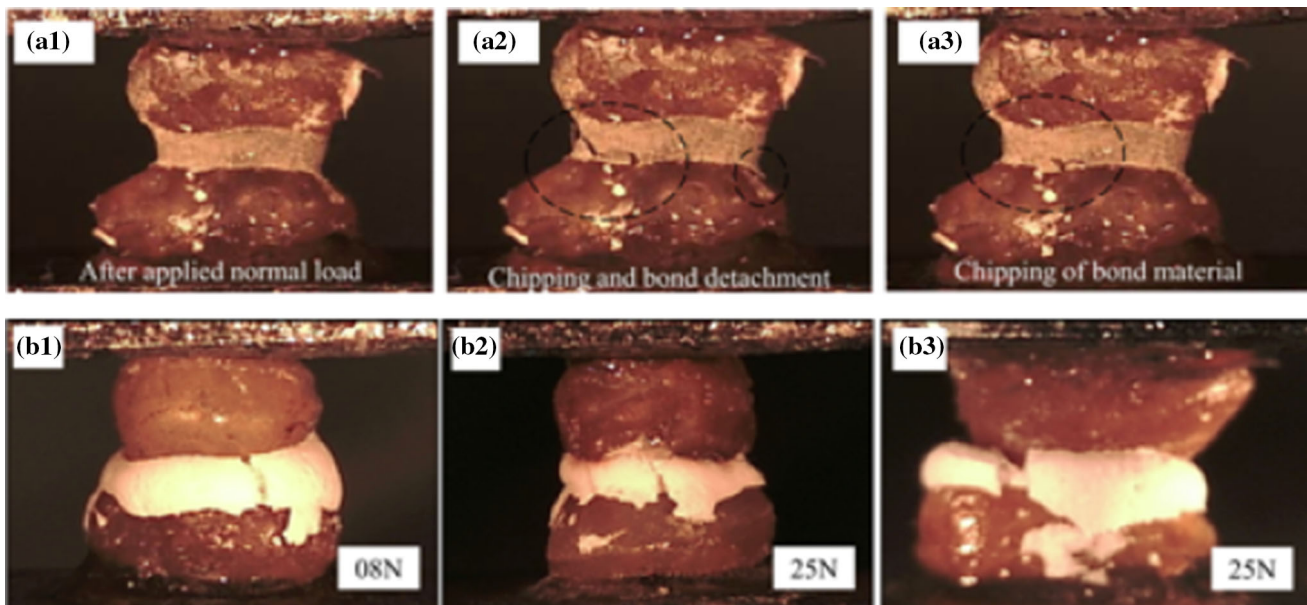
Fig. 10 **a** Stages of mode 1 failure of LBOC specimens at lower normal loads, **b** breakage phenomena at three ranges of normal loads for LBPP specimens

shows the variation of normal displacement with shearing displacement at different normal loads. The damage occurred on the specimens was crushing type with no proper shear cracks on the bonding material, and the material appeared to be squeezed out from the specimen due to the soft nature of the plaster. Wang and Leung [58] observed a similar behaviour for gypsum plaster with great volumetric contraction and bulging type of failure. Figure 10b shows representative images of specimen breakage at different normal loads for LBPP specimens.

Relating dilatancy or the rate of dilation with stress is a general mode of understanding the strength characteristics of both uncemented and cemented soils [7, 8, 42, 51]. Figure 11 shows the effects of confinement on the strength (load ratio, η) and rate of dilation (dD_N/dD_T) on LBOC specimens. At three ranges of normal loads (i.e. low, medium and high), the curves showed a decreasing load ratio, while the dilatancy rate was shifting from negative to positive values (i.e. from dilation to compression). In all the three cases, the curves ultimately reached zero dilation rate (though oscillating), but the time required to reach this condition increased at higher normal loads. At lower normal loads in pure dilation, the specimen required less time to reach zero dilation rate compared with the medium normal load range (based on the density of data points on the curve). At higher normal loads, the rate of dilation was almost constant with small fluctuations. The strength (or load ratio) of bonded sands is contributed by cohesion, dilatancy and friction components [32]. Cuccovillo and Coop [18] indicated that the energy dissipated in frictional

loss and bond breakage comprise the total work done by the stresses. The frictional loss includes the steady-state and the dilation components. However, in element-scale cemented samples, dilatancy develops under shearing after the breakage of cohesion between the grains. In the current micromechanical tests, dilatancy was observed as a consequence of breakage of the cohesion through the process of shearing as a simpler mode of energy dissipation. As the top grain is moved horizontally for shearing, the specimen tends to separate from the bonding material by breaking the bond. Since the normal load is maintained at a given constant value in a force-controlled manner, as the specimen dilates (or separates from bonding) it exerts an additional force on the loading system, making the micro-stepper motors move upwards to resume the normal load to its original values. Also, the bond does not break completely at the peak tangential load, but some bond clusters are formed [59]. These phenomena make the dilation to continue beyond the start of the steady state unlike element-scale tests. However, this occurs at lower normal loads only. At higher normal loads, the top grain will be more partial to shearing along the bond and hence dilation is not observed. This mechanism of consequent bond breakage, energy dissipation and dilation is distinct for micromechanical experiments when compared to element-scale testing. Further investigation on the interaction of shear load–normal load (and perhaps shear load–normal load–bending load) would be useful taking into account different types of bonds and bond thickness.
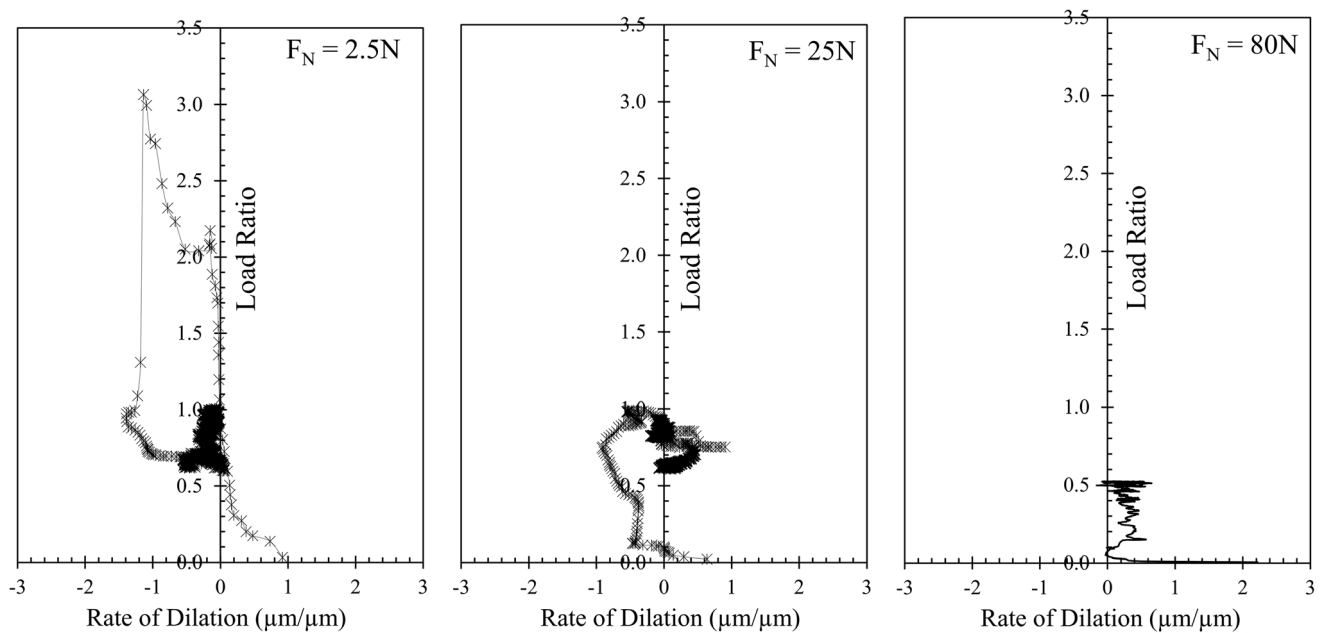
Fig. 11 Relation between load ratio and rate of dilation at low, medium and high normal loads

5 Conclusions

The study presented micromechanical tests on bonded sand-size grains investigating the tangential load–displacement behaviour in monotonic and cyclic shearing, providing insights into the failure mechanisms of the specimens and proposing an empirical expression for the failure envelope of bonded grains. The experiments were performed by upgrading and stiffening an existing micromechanical apparatus providing in this way higher precision of forces and displacements so that contact stiffness can be measured reliably. The stiffness of the apparatus was improved, and non-contact displacement transducers were used for high-precision measurements of displacements. Reproduced flat LBS grains which represent granular material with low curvature were artificially bonded with ordinary Portland cement (LBOC) and plaster of Paris (LBPP). Table 3 gives a qualitative summary of the behaviour of the bonded grains from the micromechanical tests. Monotonic shearing tests were conducted on these two classes of bonded grains in a wide range of normal loads. LBOC specimens showed higher shear strength compared to LBPP specimens, both having a nonlinear strength envelope. A new empirical nonlinear strength envelope was proposed in which the tangential load increased with decreasing rate as the normal load increased. At lower normal loads ($F_N < 20$ N), the LBOC specimens showed predominantly dilative behaviour leading to post-peak force reduction. Such specimens had

brittle failure with chipping and bond separation. At higher normal loads ($F_N > 40$ N), the LBOC specimens had compressive behaviour and the specimen failed due to crushing of the bonding material. A brittle–ductile transition was proposed to be at $F_N = 20$–25 N based on the curvature of the strength envelope, failure type and dilatant behaviour. Such distinction was not observed for LBPP specimens, and all the specimens showed compressive behaviour except for zero normal load test. The tangential stiffness also showed decreasing trend as the normal load increased, with LBOC specimen showing 2 to 3 times higher values than LBPP. The shape of stiffness degradation curves was different for LBOC specimens at lower and higher normal loads following the tangential load–displacement curves. Cyclic shearing tests on LBOC specimens showed higher energy dissipation and lower stiffness with increased displacement amplitude at a given normal load. It was observed that the energy dissipation is higher if the maximum tangential load reached in cyclic shearing is equal to the peak tangential load at a given normal load and the damage is higher in such cases if the displacement amplitude is also larger. An attempt was made to apply stress–dilatancy theory to the current micromechanical tests on LBOC specimens. The dilatancy rate was maximum at the peak tangential load, and the rate reduced as the shearing continued. From the current micromechanical tests, a mechanism of continuous mobilization of cohesion through shearing is suggested owing to the increasing dilation after steady-state sliding for bonded specimens.

Table 3 Qualitative summary of bonded grain behaviour

Specimen	Normal load (N)	Volumetric behaviour	Breakage mode		Tangential behaviour	
					Mode	Reference
LBOC (hard and strong bond)	0–16	Dilation	Chipping and specimen separation	Brittle	Softening	Figure 3a, c
	20–30	Zero dilation and post-fracture compression	Shear cracks and splitting	Brittle–ductile transition	Minor softening	Figure S1
	40–100	Compression	Crushing	Ductile	Hardening	Figure 3e
LBPP (soft and weak bond)	0	Dilation	No damage to bonding material		Softening	Figure 3b
	8–15	Compression	Crushing and squeezing of soft bonding material		Minor softening	Figure 3d
	20–60				Hardening	Figure 3f

Appendix

A Crushing load tests

Crushing tests were conducted on both LBOC and LBPP specimens using a modified CBR apparatus available at City University of Hong Kong. This apparatus was used for single-particle crushing tests on various natural geological materials like LBS and CDG [55]. A representative set of 15 samples of each LBOC and LBPP specimens were tested for crushing load. From the method of specimen preparation, it is expected that the LBOC specimens have strong and hard bond, while the LBPP specimens have weak and soft bond, and this distinct bond nature influences their crushing loads and behaviour.

Figure S2 shows the comparison of load–displacement curves between LBOC and LBPP specimens. The crushing phenomenon was straightforward for LBOC specimens where they showed brittle mode of crushing, and there was a sudden drop in the normal load after the first crack was observed, whereas the LBPP particles showed ductile behaviour with hardening to be observed even after the formation of cracks. A squeezing phenomenon was observed in the plaster as the specimen was compressed, and in both the bonding types, it was the bonding material that failed the specimen but not the LBS grains. Wang et al. [56] also observed a similar phenomenon in crushing artificially bonded LBS gains. The normal load at which the first crack occurred on the OPC-bonded particles

($F_N = 220$ N) is almost two times that of PP-bonded particles ($F_N = 114$ N), but for a given normal load below the crushing load, the displacement is always higher for LBPP than LBOC. The higher strength and stiffness for OPC-bonded particles qualifies them to be "strong and hard cementation", while the lower strength and stiffness for PP-bonded particles qualifies them to be "weak and soft cementation".

B Tensile load tests

Tensile load tests were conducted on the new micromechanical loading apparatus (Sect. 3). The top and bottom grains of the specimen were glued to the respective mounts on the apparatus with a minimum normal load applied (around 0.1 N) to ensure firm contact between the specimen and the mounts. After the preparation of the cemented samples, the extension tests were conducted to measure the tensile strength of the specimens. In general, these tests showed a brittle behaviour with a sudden drop of the load after reaching a peak value. The average tensile load at which the bond breakage occurred for LBOC specimens was 1.71 N, and the breakage occurred at a very low extension of around 1.25 µm indicating the brittle nature of the bond. The normal load–extension curve for a representative specimen is shown in Figure S3, while the LBPP particles did not show any recordable tensile load during the separation of the bonding.

References

1. Acar YB, El-Tahir AE (1986) Low strain dynamic properties of artificially sands. J Geotech Eng ASCE 112(11):1001–1015
2. Alvarado G, Lui N, Coop MR (2012) Effect of fabric on the behaviour of reservoir sandstones. Can Geotech J 49(9):1036–1051

3. Anagnostopoulos AG, Kalteziotis N, Tsiambaos GK, Kavvadas M (1991) Geotechnical properties of the Cornith Canal marls. Geotech Geol Eng 9(1):1–26

4. Atkinson J (1993) An introduction to the mechanics of soils and foundations. McGraw-Hill international series in civil engineering. McGraw-Hill, New York

5. Barton N (1976) The shear strength of rock and rock joints. Int J Rock Mech Min Sci Geomech Abstr 13(9):255–279

6. Barton N (2016) Non-linear shear strength for rock, rock joints, rockfill and interfaces. Innov Infrastruct Solut 1:30

7. Been K, Jefferies M (2004) Stress-dilatancy in very loose sand. Can Geotech J 41:972–989

8. Bolton MD (1986) The strength and dilatancy of sands. Geotechnique 20(1):65–78

9. Byerlee JD (1968) Brittle–ductile transition in rocks. J Geophys Res 73:4741–4750

10. Chang CS, Kabir MG (1994) Mechanics for brittle and ductile behavior of cemented sands. In: Proceedings of XIII ICSMFE, New Delhi, pp 369–372

11. Cheung LYG, O'Sullivan C, Coop MR (2013) Discrete element method simulations of analogue reservoir sandstones. Int J Rock Mech Min Sci 63:93–103

12. Chiu CC, Weng MC, Huang TH (2015) Biconcave bond model for cemented granular material. J GeoEng 10(3):91–103

13. Clough GW, Iwabuchi J, Rad NS, Kuppusamy T (1979) Silicate-stabilized sands. J Geotech Eng ASCE 105(1):65–82

14. Clough GW, Sitar N, Bachus RC (1981) Cemented sand under static loading. J Geotech Eng Div ASCE 107(6):799–817

15. Consoli NC, Foppa D, Festugato L, Heineck KS (2007) Key parameters for strength control of artificially cemented soils. J Geotech Geoenviron Eng 133(2):197–205

16. Coop MR, Atkinson JH (1993) The mechanics of cemented carbonate sands. Géotechnique 43(1):53–67

17. Coop MR, Wilson SM (2003) Behaviour of hydrocarbon reservoir sands and sandstones. J Geotech Geoenviron Eng 129(11):1010–1019

18. Cuccovillo T, Coop MR (1999) On the mechanics of structured sands. Geotechnique 49(6):741–760

19. Cui MJ, Zheng JJ, Zhang RJ, Lai HJ, Zhang J (2017) Influence of cementation level on the strength behaviour of bio-cemented sand. Acta Geotech 12:971–986

20. Das A, Tengattini A, Nguyen G, Einav I (2013) A micromechanics based model for cemented granular materials. In: Yang Q et al (eds) Constitutive modeling of geomaterials, Springer Serier in Geomechanics Geoengineering pp. Springer, Berlin, Heidelberg, pp 527–534. https://doi.org/10.1007/978-3-642-32814-5_71

21. de Bono J, McDowell G, Wanatowski D (2015) Investigating the micro mechanics of cemented sand using DEM. Int J Numer Anal Methods Geomech 39(6):655–675

22. Duan K, Kwok CY, Ma X (2017) DEM simulations of sandstone under true triaxial compressive tests. Acta Geotech 12:495–510

23. Haeri SM, Hamidi A, Hosseini SM, Asghari E, Toll DG (2006) Effect of cement type on the mechanical behaviour of a gravely sand. Geotech Geol Eng J 24(2):335–360

24. Haeri SM, Hosseini SM, Toll DG, Yasrebi SS (2005) The behaviour of an artificially cemented sandy gravel. Geotech Geol Eng J 23(5):537–560

25. Hamidi A, Haeri SM (2008) Stiffness and deformation characteristics of a cemented gravely sand. Int J Civ Eng 6(3):159–173

26. Hoek E, Brown ET (1980) Empirical strength criterion for rock masses. J Geotech Eng Div ASCE 106(9):1013–1025

27. Hoek E, Brown ET (1988) The Hoek–Brown failure criterion—a 1988 update. In: Proceedings of the 15th Canadian rock mechanics symposium, pp 31–38

28. Jiang MJ, Jin SL, Shen ZF, Liu W, Coop MR (2015) Preliminary experimental study on three-dimensional contact behavior of bonded granules. IOP Conf Ser Earth Environ Sci 26(1):012007

29. Jiang MJ, Sun YG, Li LQ, Zhu HH (2012) Contact behaviour of idealized granules bonded in two different interparticle distances: an experimental investigation. Mech Mater 55:1–15

30. Lade PV, Overton DD (1989) Cementation effects in frictional material. J Geotech Eng ASCE 115:1373–1387

31. Lade PV, Yamamuro JA (1996) Undrained sand behaviour in axisymmetric tests at high pressures. J Geotech Eng ASCE 122(4):309–316

32. Lambe TW (1960) A mechanical picture of shear strength in clay. In: Research conference on shear strength of cohesive soils. University Colorado Press, Boulder, CO, pp 555–580

33. Leroueil S, Vaughan PR (1990) The general and congruent effects of structure in natural soils and weak rocks. Geotechnique 40(3):467–488

34. Li Z, Wang YH, Ma CH, Mok CMB (2017) Experimental characterization and 3D DEM simulation of bond breakages in artificially cemented sands with different bond strengths when subjected to triaxial shearing. Acta Geotech 12:987–1002

35. Lo SCR, Lade PV, Wardani SPR (2003) An experimental study of the mechanics of two weakly cemented soils. Geotech Test J 26(3):328–341

36. Menendez B, Zhu W, Wong TF (1996) Micromechanics of brittle faulting and cataclastic flow in Brea sandstone. J Struct Geol 18(1):1–16

37. Mitchell J, Soga K (2005) Fundamentals of soil behaviour, 3rd edn. Wiley, New York

38. Mogi K (1966) On the pressure dependence of strength of rocks and the Coulomb fracture criterion. Tectonophysics 21(3):273–285

39. Muir Wood D (2007) Soil behaviour and critical state soil mechanics. Cambridge University Press, Cambridge

40. Nardelli V, Coop MR (2019) The experimental contact behaviour of natural sands: normal and tangential loading. Geotechnique 69(8):672–686

41. Rios S, da Fonseca AV, Baudet BA (2014) On the shearing behaviour of an artificially cemented soil. Acta Geotech 9:215–226

42. Rowe PW (1962) The stress-dilatancy relation for static equilibrium of an assembly of particles in contact. Proc R Soc Lond A 269:500–527

43. Rowe PW, Oates DB, Skermer NA (1964) The stress-dilatancy performance of two clays. In: STP361-EB Laboratory shear testing of soils pp 134–146. ASTM International. https://doi.org/10.1520/STP29990S

44. Sandeep CS, Senetakis K (2018) Grain-scale mechanics of quartz sand under normal and tangential loading. Tribol Int 117:261–271

45. Santamarina JC, Klein A, Fam MA (2001) Soils and waves: particulate material behaviour, characterization and process monitoring. J Soils Sedim 1(2):196

46. Saxena SK, Lastrico RM (1978) Static properties of lightly cemented sand. J Geotech Eng Div ASCE 4(12):1449–1464

47. Schnaid F, Prietto PDM, Consoli NC (2001) Characterization of cemented sand in triaxial compression. J Geotech Geoenviron Eng 127(10):857–868

48. Senetakis K, Coop MR, Todisco MC (2013) Tangential load-deflection behaviour at the contact of soil particles. Geotech Lett 3(2):59–66

49. Shen B, Shi J, Barton N (2018) An approximate nonlinear modified Mohr–Coulomb shear strength criterion with critical state for intact rocks. J Rock Mech Geotech Eng 10:645–652

50. Shi Z, Jiang T, Jiang M, Liu F, Zhang N (2015) DEM investigation of weathered rocks using a novel bond contact model. J Rock Mech Geotech Eng 7:327–336
51. Taylor DW (1948) Fundamentals of soil mechanics. Wiley, New York
52. Terzis D, Laloui L (2019) Cell-free soil bio-cementation with strength, dilatancy and fabric characterization. Acta Geotech 14:639–656
53. Tian Y, Liu Q, Ma H, Liu Q, Deng P (2018) New peak shear strength model for cement filled rock joints. Eng Geol 233:269–280
54. Trivedi A (2010) Strength and dilatancy of jointed rocks with granular fill. Acta Geotech 5:15–31
55. Wang W, Coop MR (2016) An investigation of breakage behaviour of single sand particles using a high-speed microscope camera. Geotechnique 66(12):984–998
56. Wang W, Coop MR, Senetakis K (2019) The development of a micromechanical apparatus applying combined normal–shear–bending forces to natural sand grains with artificial bonds. Geotech Test J 42(4):1090–1099. https://doi.org/10.1520/GTJ20170453
57. Wang W, Nardelli V, Coop MR (2017) Micro-mechanical behaviour of artificially cemented sands under compression and shear. Geotech Lett 7:218–224
58. Wang YH, Leung SC (2008) A particulate-scale investigation of cemented sand behaviour. Can Geotech J 45(1):29–44
59. Wang YH, Leung SC (2008) Characterization of cemented sand by experimental and numerical investigations. J Geotech Geoenviron Eng 134(7):992–1004
60. Wong TF, Baud P (2012) The brittle–ductile transition in porous rock: a review. J Struct Geol 44:25–53
61. Wu S, Zhang S, Guo C, Xiong L (2017) A generalized nonlinear failure criterion for frictional materials. Acta Geotech 12:1353–1371
62. Yu HS, Tan SM, Schnaid F (2007) A critical state framework for modelling bonded geomaterials. Geomech Geoeng Int J 2(1):61–74